Maximized Hydrodynamic Stimulation Strategy for Placement of Differential Pressure and Velocity Sensors in Artificial Lateral Line Systems

Zhen Yang, Zheng Gong, Yonggang Jiang, Yueri Cai, Zhiqiang Ma, Xin Na, Zihao Dong, and Deyuan Zhang

***Abstract*—Fish can perceive the surrounding flow field using their lateral line systems, consisting of canal neuromasts (CNs) for flow pressure gradient perception and superficial neuromasts (SNs) for flow velocity detection. Although various artificial lateral line (ALL) systems have been developed inspired by the lateral line of fish, few studies have combined both pressure and velocity sensors for hydrodynamic perception, and how to optimize sensor placement remains unanswered, particularly on three-dimensional models. Herein we proposed a maximized hydrodynamic stimulation strategy for sensor placement optimization. We built a fish model and designed an ALL system by mimicking the geometry of a blind cavefish, *Sinocyclocheilus tianlinensis*. Differential pressure sensors and hot-film flow velocity sensors were used to mimic the CNs and SNs, respectively, with optimized sensor placement. The simulation and experimental results on yaw angle detection suggested that both sensor placement of our ALL system and distribution of the biological lateral line showed good agreement with the maximized hydrodynamic stimulation strategy. Our ALL system could detect a wall within a distance of 0.1 body length, comparable to the perception ability of cave fish. The new sensor placement strategy can be used to equip ALL systems on bionic robotic fish and other underwater vehicles.**

***Index Terms*—Biomimetics, sensor fusion, artificial lateral line, sensor placement.**

I. Introduction

FISH possess a unique lateral line system, which enables them to perceive information about the surrounding flow field and facilitate many physiological activities, such as prey tracking, obstacle avoidance, and schooling. The basic sensing units of the lateral system are the neuromasts, which are distributed all over the fish body. Depending on their function and distribution, neuromasts are classified into two types: canal neuromasts (CNs) under the subepidermal lateral line canals, and superficial neuromasts (SNs) on the surface of fish. CNs are sensitive to the pressure gradients between adjacent canal pores on the lateral line canals, while SNs are in direct contact with water and are sensitive to the local flow velocity [1]. Although the distribution and number of neuromasts are different in different fish species, cave fish generally have a more developed and sensitive lateral line system than surface fish to compensate for the lack of vision [2], [3].

Inspired by the flow perception capability of biological lateral lines, many artificial lateral line (ALL) systems, consisting of various types of sensors, have been developed for different applications. The most common applications are dipole-source detection and hydrodynamic sensing. Because the flow fields generated by a dipole are similar to those generated by fins and insects, many studies have used the ALL systems to detect dipole sources [4], [5]. For hydrodynamic sensing, ALL systems were used for identifying flow field characteristics like flow regimens [6] and for detecting pressure [7], flow velocity [8], and yaw angles [9]. Various sensors were employed to mimic the neuromasts on the lateral line, but most of the before-mentioned studies have adopted only a single pressure- or velocity-sensing modality. In our previous study, we first utilized a sensor fusion modality to localize an underwater target by combing pressure and flow sensors [10]. One of the main difficulties of ALL systems with multimodal sensors lies in sensor placement.

Most of the aforementioned studies adapted a simple sensor placement following engineering intuition, where the ALL system comprises one or two sets of aligned sensors with uniform spacing [5], [10], [11]. For the practical application of the ALL system, sensor placement should be simplified and optimized. However, limited studies have focused on sensor placement. Xu *et al.* proposed some optimal methods based on optimal weight analysis, feature importance, and information redundancy to place pressure sensors in a wing-shaped model [12], [13]. Weber *et al.* employed a Bayesian experimental design and numerical simulations of the two-dimensional (2D) Navier-Stokes equations to optimize sensor distribution in a 2D slender deforming

Manuscript received September 9, 2021; accepted December 31, 2021. Date of publication January 14, 2022; date of current version January 25, 2022. This letter was recommended for publication by Associate Editor Y. Chen and Editor X. Liu upon evaluation of the reviewers' comments. This work was supported by the National Natural Science Foundation of China under Grants 51975030 and 52022008. *(Zhen Yang and Zheng Gong are co-first authors.) (Corresponding author: Yonggang Jiang.)*

The authors are with the School of Mechanical Engineering and Automation, Beihang University, Beijing 100191, China (e-mail: yangzhen@buaa.edu.cn; zhenggong@buaa.edu.cn; jiangyg@buaa.edu.cn; caiyueri@buaa.edu.cn; mazqbuaa@163.com; nx2020@buaa.edu.cn; haulmess@buaa.edu.cn; zhangdy@buaa.edu.cn).

Digital Object Identifier 10.1109/LRA.2022.3143203

2377-3766 © 2022 IEEE. Personal use is permitted, but republication/redistribution requires IEEE permission.
See https://www.ieee.org/publications/rights/index.html for more information.

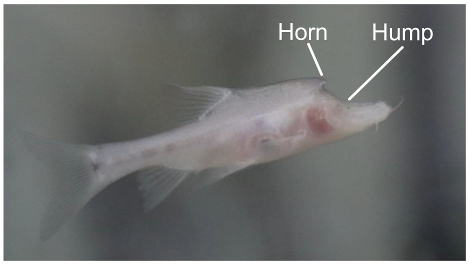

Fig. 1. Blind cave fish *Sinocyclocheilus tianlinensis*.

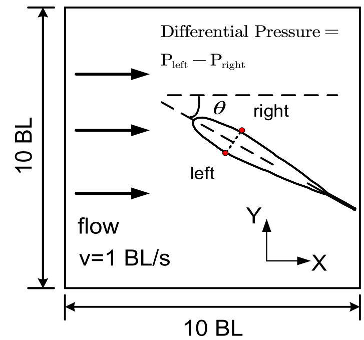

Fig. 2. Schematics of hydrodynamic simulation (top view). θ: yaw angle of the fish body relative to the incoming flow.

shape swimmer [14]. However, these studies were based on simple 2D streamline models for analysis; the findings from a 2D setting cannot directly be generalized for a three-dimensional (3D) setting. Ahrari *et al.* proposed two design concepts, viz. "offset strategy" and "angle strategy", to overcome the challenge of blind regions in 3D dipole source detection; however, their model was also a 2D stretched streamline body [15]. The 3D models of robotic fish are more complex than wing-shape models and cannot be easily described directly using mathematical models, which makes it difficult to generalize the above optimization algorithms in high dimensions. Some ALL systems on robotic fish were just placed around the bodies, without considering the optimization of the layout in 3D space [16], [17].

In this letter, we propose a maximized hydrodynamic stimulation strategy to place sensors on 3D models, according to which sensors are placed at the locations where the hydrodynamic parameters change most obviously. The results of yaw simulation and experiments show good agreement with the distribution of biological lateral lines. We designed an ALL system by integrating differential pressure sensors and flow velocity sensors to mimic CNs and SNs on a cave fish model. The ALL system showed enhanced capability for hydrodynamic perception, such as yaw angle sensing and wall detection.

II. Sensor Placement

A. Bionic Prototype

We chose the Chinese blind cavefish *Sinocyclocheilus tianlinensis* as a bionic prototype. *S. tianlinensis* is a typical cave fish with typical troglomorphic traits in cavefish, such as absence of eyes and enhanced mechanosensation and chemosensation [18]. One of the prominent physical features of *S. tianlinensis* is the dorsal hump and horn [19] as shown in Fig. 1. The main reason for selecting *S. tianlinensis* is that it has a well-developed lateral line system. In our previous studies, we found that the lateral line systems of two species of *Sinocyclocheilus* have constriction canal structures, which can increase the sensitivity of the lateral line system [20]. Eyeless *S. tianlinensis* has a more sensitive lateral line than eyed cave fish to compensate for the lack of eyes [21].

Since *S. tianlinensis* has a well-developed lateral line system, we mimicked its distribution of neuromasts to optimize sensor placement on the ALL system. We investigated the distribution and microstructures of the lateral line system of *S. tianlinensis*, and found that the distribution of the cephalic canal lateral line system is affected by fish body shape [21]. A bionic fish model was designed based on an *S. tianlinensis* specimen to better fit the geometric characteristics of the lateral line. A high-fidelity 3D model was obtained by scanning the specimen, and the caudal and ventral fins were removed. To facilitate simulation and production, we smoothed the fish model and made it symmetrical. After equal-scale enlargement, a bionic *S. tianlinensis* model with a body length (BL) of 22 cm was obtained. The relationship between sensor placement and hydrodynamic stimulation was studied using the bionic fish model.

B. Hydrodynamic Simulation

Mediating the yaw angle is an important function for a fish or a robotic fish, as it allows fish to travel with the current, which helps save energy [22]. We expect the ALL system to assist the robotic fish in adjusting the yaw angle to swim more efficiently and avoid obstacles; therefore, our sensor placement should characterize the angle of fish relative to the incoming flow.

We utilize differential pressure sensors to mimic CNs and hot-film flow velocity sensors to simulate SNs. The reasons for using these sensors are introduced in the next section. Our sensor placement strategy involves placing the sensors where the hydrodynamic stimulation (differential pressure or wall shear stress) changes significantly on the surface of the ALL model, which is called the maximized hydrodynamic stimulation strategy, to improve the signal-to-noise ratio of the sensor and allow the ALL system to distinguish different working conditions accurately. Differential pressure sensors are used to measure the differential pressure at the symmetrical locations of the fish model, which should be placed in the area where the differential pressure changes most significantly. Flow velocity sensors are used to measure wall shear stresses along the body length, which should be attached to the surface where the wall shear stress varies most prominently along the body length. Owing to the existence of a laminar boundary layer, wall shear stress is the main stimulus to the surface, and wall shear stress along the body length can be approximated as a stimulus to SNs [23].

Yaw angle simulations were performed to calculate the regions of maximized hydrodynamic stimulation through computational fluid dynamics (CFD). As shown in Fig. 2, a flow domain

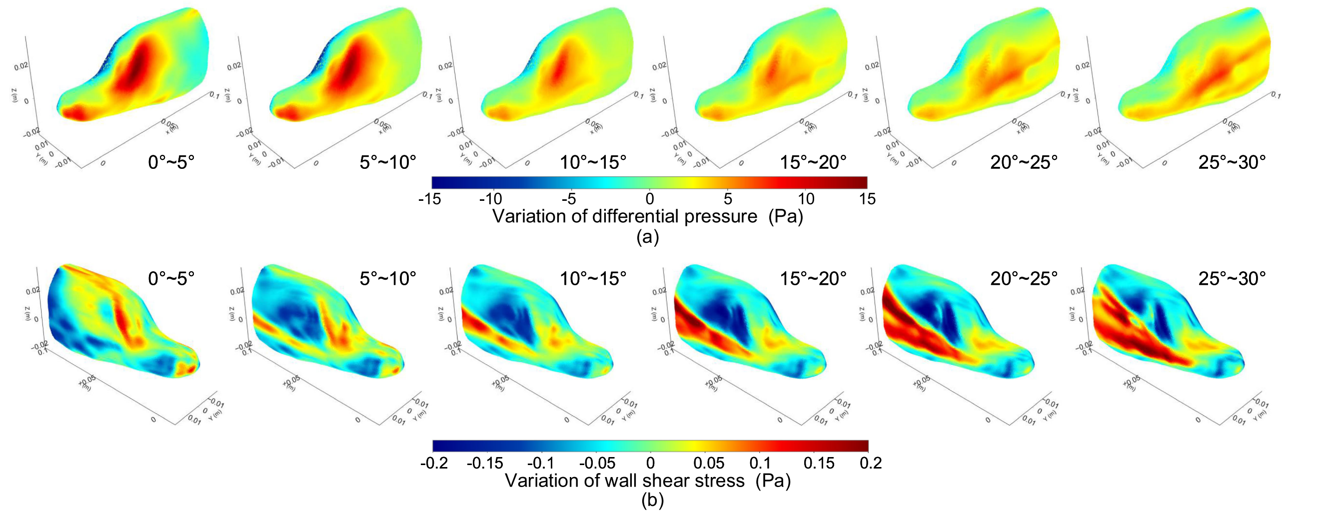

Fig. 3. Contours of the variation of differential pressure (a) and wall shear stress (b) by subtracting simulation result with yaw angle of 5° difference (0° ∼ 5° means the variation from 0° to 5°). The most obvious regions of differential pressure and wall shear stress change are at the nose, hump, and side.

with a domain size of $10 \times 10 \times 10$ BL was used to simulate the open water, and the fish model was placed in the center of the domain. The simulations were conducted in a steady flow, and the constant incoming flow velocity was 1 BL/s. The differential pressure at a point is defined as the pressure at the point minus the pressure at the symmetrical point (the differential pressure of the left point is shown as Fig. 2). The hydrodynamic parameters of the fish surface at different yaw angles were obtained by changing the yaw orientation θ of the fish body relative to the incoming flow.

The lateral line system of fish is usually concentrated in the first 20% of the body length, and the pressure distribution is significantly affected only for the leading 20% of the body when approaching a wall [24], [25]. Sensors are usually placed on the head if the ALL system is installed on a robotic fish. Therefore, we analyzed the simulation results of the head. We extracted the simulation results with θ of 0°, 5°, 10°, 15°, 20°, 25°, and 30° and subtracted the data of adjacent 5° (e.g., data of 5° subtracted data of 0°) to obtain the changes in differential pressure and wall shear stress.

The variation in the differential pressure of the flow-facing (left) side is shown in Fig. 3(a). When the yaw angle is small (0°∼ 15°), the most obvious areas of differential pressure change are at the nose and hump. As the yaw angle increases, the peak of the differential pressure changes decreases, and the region with the most obvious change gradually moves toward the side of the fish. However, the most obvious regions of wall shear stress variation are concentrated on the leeward (right) side (Fig. 3(b)). Similarly, the largest variation occurs at the nose and hump, and the regions of great shear stress variation move toward the side as the yaw angle increases. Therefore, placing the sensors at the nose, hump, and the side of the fish allows the ALL systems to collect signals with more significant changes when the yaw angle changes and improves the signal-to-noise ratio.

The regions with the maximum hydrodynamic stimulation obtained from the simulation results were highly similar to the lateral line distribution of *S. tianlinensis* (Fig. 4). The regions

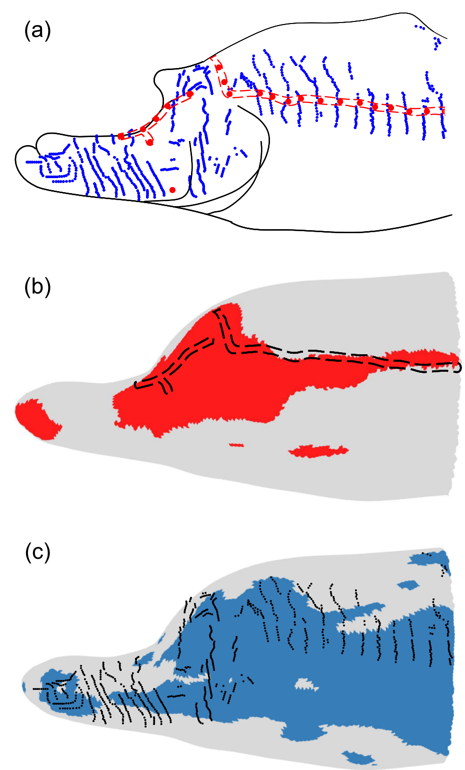

Fig. 4. Regions with the maximized hydrodynamic stimulation are similar to the lateral line distribution of *S. tianlinensis*. (a) SNs (blue circles), CNs (red circles), and lateral canals (red line) distribution of *S. tianlinensis*. (b) Regions with maximum differential pressure variation (red) and lateral canals (black line). (c) Regions with maximum wall shear stress variation (blue) and SNs (black circles).

with the top 10% largest variations in differential pressures shown in Fig. 3(a) were combined to obtain the red area shown in Fig. 4(b), which completely covered the lateral line canals and CNs. Similarly, we combined the union of regions with the top 10% largest variations in wall shear stress from Fig. 3(b), and it covers most SNs on the nose and side of its body (Fig. 4(c)).

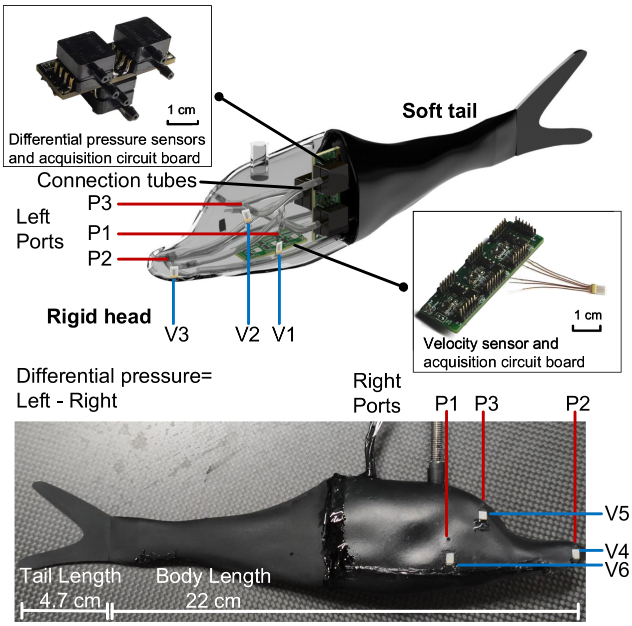

Fig. 5. Hardware configurations of fish model and the sensor distribution of the ALL system.

Although the shape and lateral line distribution of each fish are slightly different, and the smoothed fish model loses some morphological details, the results indicate that optimized sensor placement based on our maximized hydrodynamic stimulation strategy is consistent with the biological lateral line distribution.

C. Experimental Platform

We optimized the sensor placement based on simulation results obtained using the maximized hydrodynamic stimulation strategy. The sensor placement area can be obtained through our strategy, but the specific placement positions need to be adjusted according to the sensor size and model shape. In our ALL system, sensors were placed at the intersection of areas with significant parameter variations at different angles, making multiple sensors change significantly at each angle. As fish always have many SNs near the lateral line canal [21], our ALL system mimicked this characteristic by arranging the ports of differential pressure sensors and flow velocity sensors in adjacent locations near the biological lateral line. Fig. 5 illustrates the final ALL system. Six flow velocity sensors were placed symmetrically at the nose, hump, and side, and six connection holes for three differential pressure sensors were placed next to the flow velocity sensors.

The differential pressure sensors (MPXV7002DP, NXP) were placed inside the fish model and connected to ports on the rigid head using silicone connection tubes. The medium in the connection tubes was air. Two symmetrical ports were connected to a differential pressure sensor to measure the differential pressure at symmetrical positions. Most artificial lateral line systems are equipped with absolute pressure sensors [10], [26], [27]; however, ALL systems based on absolute pressure sensors suffer from a few limitations, which limit their usability at large depths. For example, the static component of pressure necessitates large pressure ranges, rendering them incompatible with high sensitivities [9]. The differential pressure sensors adapt to a wider range of depths [28].

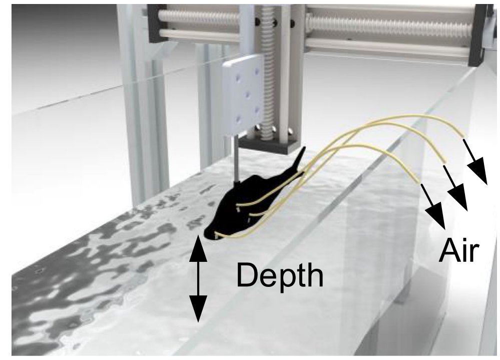

Fig. 6. Calibration of the differential pressure sensors. Change the depth in the water to calculate the sensitivity of sensors.

The hot-film flow velocity sensors (FS2T.0.1E.025, IST) were attached to the surface of the rigid head and connected to the acquisition circuit board using shielded wires. Hot-film flow velocity sensors are typically stable and sensitive [29]. Although FS2 flow sensors are applicable in gas, we tested them and found that they also work well underwater.

Considering that the system will be used on a robotic fish in the future, the fish model has a rigid head and a soft tail for joint movement. The analog signals of the nine sensors were read by a data acquisition card (USB-4711 A, Advantech Co.), and processed in LabView.

III. Experiments and Results

A. Sensor Calibration

All sensors were calibrated in the laboratory before the experiments. As shown in Fig. 6, one port of each differential pressure sensor was connected to the air through a silicone tube, and the other port was connected to the water. The voltage U_0 at zero differential pressure was measured in air. Then, the fish model was sunk into the water, and the sensitivity of the differential pressure sensors was calculated by adjusting the water depth. The output voltage of the sensors exhibits a linear relationship with pressure variation. Fig. 7 shows the calibration result for a sensor P2, which measured the differential pressure at the nose.

The wall shear stress τ_ω generated by the flow is expressed as follows:

$$\tau_\omega = \mu \frac{\mathrm{d}U}{\mathrm{d}y}\bigg|_{y=0} \tag{1}$$

where μ is the dynamic viscosity of fluid, $\mathrm{d}U/\mathrm{d}y$ is the mean streamwise velocity gradient at the wall. As the output voltage of the hot-film sensors varies with changes in the velocity gradient in the boundary layer. And τ_ω is positively correlated with velocity gradient. Thus, the output voltage calibrated by incoming flow velocity can reflect the variation in wall shear stress [30].

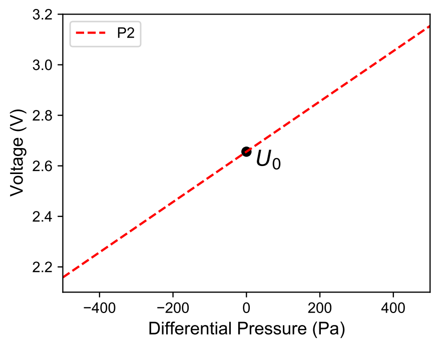

Fig. 7. The differential pressure sensors exhibit a linear relationship between differential pressure and voltage. U_0: voltage at zero differential pressure.

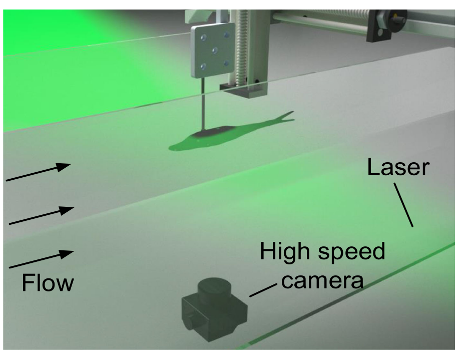

Fig. 8. Calibration of the velocity sensors with a PIV system.

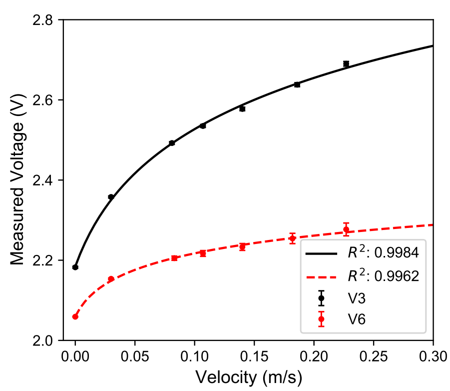

Fig. 9. The flow velocity sensors exhibit a logarithmic relationship between velocity and voltage. The output voltage can reflect the variation of wall shear stress.

A particle image velocimetry (PIV) system was used to calibrate the flow velocity sensors in a circulating water tunnel, as shown in Fig. 8. The laser irradiated the plane perpendicular to the sensor, and a high-speed camera at the bottom recorded the movements of the particles near the sensor. Because hot-film sensors are highly sensitive to temperature, it is essential to avoid laser irradiation of the sensing unit directly. Taking V3 and V6 as examples, the output voltage exhibits a logarithmic relationship with the flow velocity, with a goodness of fit larger than 0.996 (Fig. 9). As the relationship between the voltage output and flow velocity is logarithmic, the voltage difference cannot be used to calculate the flow velocity difference. Therefore, we directly considered the output voltage of the flow velocity sensors as a signal to reflect the variance of the flow velocity and wall shear stress.

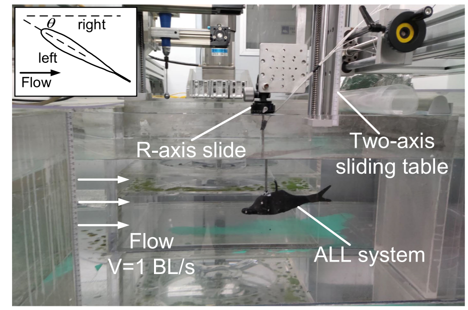

Fig. 10. Setup for yaw angle experiments.

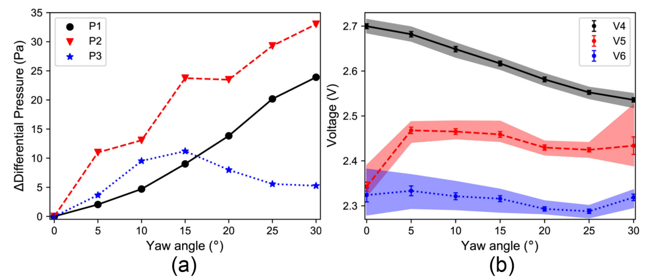

Fig. 11. Results of yaw angle experiments. θ: yaw angle of the fish body relative to the incoming flow. (a) Variation of differential pressure at different yaw angles. (b) The output voltage of flow velocity sensors at different yaw angles. The shaded areas show the voltage fluctuation range (minimum voltage to maximum voltage).

B. Yaw Angle Experiments

To verify the effectiveness of the maximized hydrodynamic stimulation strategy, yaw angle experiments were conducted. As shown in Fig. 10, the fish model was placed in a circulating water tunnel with an experimental section of $70{\times}35{\times}40$ cm, and the water depth was 30 cm. The flow velocity generated by the water tunnel was almost constant. The fish model was connected to a two-axis sliding table and moved to the center of the tunnel. The top of the model was placed 10 cm away from the water surface to reduce the impact of water surface fluctuations. The angle θ between the model and the flow was adjusted using an R-axis slide. The sensor data were collected at the yaw angle of 0°, 5°, 10°, 15°, 20°, 25°, and 30° under an incoming flow at a speed of 1 BL/s, which was the same speed as simulation.

The experimental results were compared with the simulation results, and the differential pressure sensors and flow velocity sensors on the leeward (right) side were analyzed. The differential pressure at 0° was taken as a reference point, and the change in differential pressure at other angles relative to 0° was recorded as Δdifferential pressure. As shown in Fig. 11(a), as the yaw angle increases, the differential pressures of P1 (side) and P2 (nose) gradually increase, which is in good agreement with the simulation results. P3 (hump) starts to fall after 15°, probably caused by the movement of the regions with the most obvious differential pressure variation. As for the flow velocity sensors

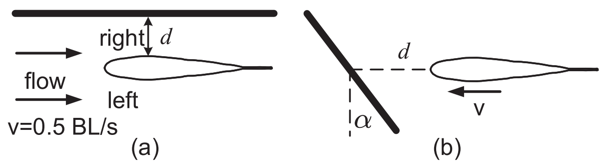

Fig. 12. Experimental schematics for wall detection. d is the distance from the wall, and α is the angle of rotation of the wall. (a) Passive hydrodynamic imaging. (b) Active hydrodynamic imaging.

(Fig. 11(b)), the output voltage of V4 (nose) decreases as the yaw angle increases, which exhibits a good linear relationship. The output voltage of V5 (hump) increased at 5° and then tended to decrease, but increased slightly at 30°. These two flow velocity sensors are generally consistent with the tendency of the simulation. However, the voltage of V6 (side) tends to rise after 25°, instead of starting to rise at 5° in the simulation, which is probably due to the reflux applied on the leeward side. When the yaw angle is less than 20°, the voltage output of V6 (blue area) shows a large fluctuation, which also indicates a significant effect of reflux. The inconsistency of V5 with simulation occurs at 30°, where the voltage fluctuation (red area) is also significant. In conclusion, the yaw angle experimental results at the nose and hump are consistent with the simulation. The yaw angle can be easily predicted using the sensors on the nose (V4, P2), and the voltage fluctuations of the flow sensors can also help to predict.

C. Wall Detection

Blind cave fish use their lateral line systems for hydrodynamic imaging, which helps them avoid rugged walls and swim freely in dark caves. There are two types of hydrodynamic imaging: passive hydrodynamic imaging, where fish perceive fluid flow generated externally, and active hydrodynamic imaging, where fish use flow field generated by their movement to detect stationary obstacles [31]. We designed both passive and active experiments to evaluate the hydrodynamic imaging ability of our ALL system for wall detection.

Fig. 12(a) schematically illustrates the passive hydrodynamic imaging experiment. The fish model was placed in the circulating water tunnel, similar to that in the yaw angle experiment, and the distance from the wall of the tunnel was adjusted by a two-axis sliding table. Under a constant incoming flow (0.5 BL/s), the sensor data of the ALL system were collected at different wall distances d to detect the wall. We took the differential pressure in the case of d=5 cm (0.23 BL) as the initial differential pressure and subtracted this value to obtain the change in differential pressure (Δdifferential pressure). For the sake of illustration, the value of Δdifferential pressure was inverted. As shown in Fig. 13(a), the pressure on the right side, which is close to the wall, tends to rise when approaching the wall, with significant change at 0.1 BL and 0.02 BL away from the wall. At the same time, the voltage of V6 (right side) also has a significant increase at 0.02 BL, and the voltage of V4 (right nose) decreases slowly within 0.1 BL (Fig. 13(b)).

Fig. 12(b) depicts the principle of the active hydrodynamic imaging experiment. The fish model was attached to the slide by

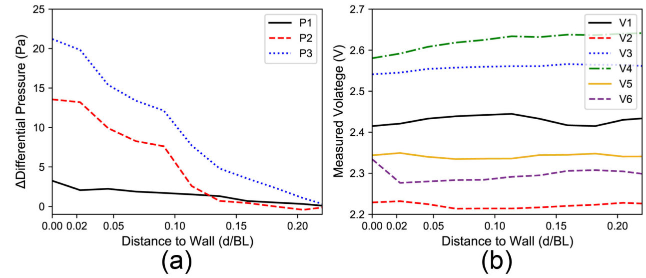

Fig. 13. The passive hydrodynamic imaging results when the fish model is at different distances from the wall. (a) Variation of differential pressure when taking the reference differential pressure at the distance of 0.23 BL. The differential pressures gradually increase when d is decreasing. (b) The output voltage of flow velocity sensors.

a rod and moved at different speeds toward a wall. The maximum gliding speed was set to 1 BL/s, covering the speeds of most robotic fish [32]. An acrylic plate was placed 1.2 BL away from the model, and the angle α of the plate could be varied through an R-axis slide. Compared with passive hydrodynamic imaging, the noise caused by mechanical vibrations resulting from the separation of the flow surrounding the rods was much more significant in the active hydrodynamic imaging experiments. Positively, this noise will be reduced when the robotic fish is swimming in the water without a rod. As the differential pressure sensors were significantly affected by mechanical vibrations when sliding, we only analyzed the data from flow velocity sensors for active wall detection. Because the fluctuations of the two symmetrical flow velocity sensors were similar, we reduced the noise by processing the measurement voltage of flow velocity sensors on the symmetrical plane as follows:

$$\begin{aligned} V_{left}^{(i)} - V_{right}^{(i)} &= (V_{left\_measured}^{(i)} - V_{right\_measured}^{(i)}) \\ &\quad - \frac{1}{n}\sum_{i=1}^{n}(V_{left\_measured}^{(i)} - V_{right\_measured}^{(i)}) \end{aligned} \tag{2}$$

where, $V_{left\_measured}^{(i)} - V_{right\_measured}^{(i)}$ denotes the difference between the measured voltages of the two symmetrical flow velocity sensors under the moment of i. After subtracting the average value, $V_{left}^{(i)} - V_{right}^{(i)}$ is approximately zero. We analyzed the processed data V1-V6 (side), V2-V4 (hump), and V3-V4 (nose).

The results demonstrated that the flow velocity sensors at the nose could detect the wall. As shown in Fig. 14, when the distance from the wall is between 0.05 BL and 0.1 BL, the value of V3-V4 increases, owing to the increase in the measured voltage of V3 (left nose). At the same sliding speed (0.1 BL/s), the peak value of V3-V4 increases with α (Fig. 14(a)–(c)); however, the variation is negligible at a small angle of 15° (Fig. 14(a)). Although the sliding speed is slow, the sensors can still respond to the wall within a distance of 0.1 BL. At the same α=45°, after the speed exceeds 0.1 BL/s, although the impact increases with speed, the value of V3-V4 still varies at a distance of about 0.1 BL, not significantly increasing in advance (Fig. 14(d)).

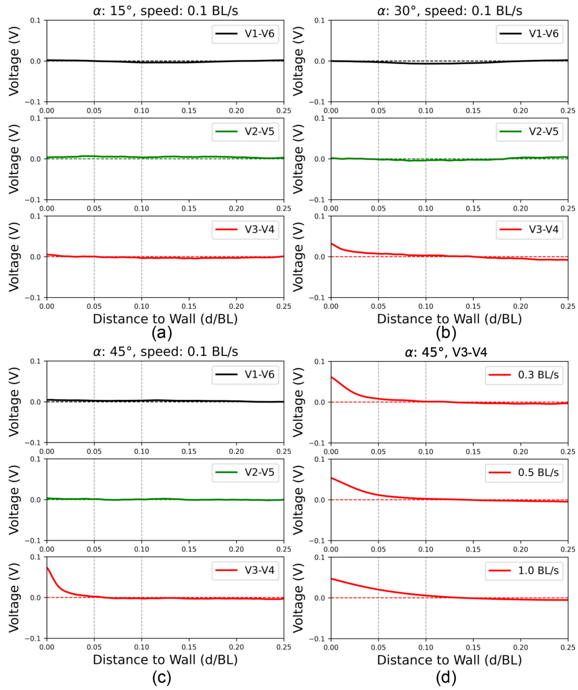

Fig. 14. The active hydrodynamic imaging results when approaching a wall (d is decreasing). (a)–(c) At the same sliding speed of 0.1 BL/s, the peak voltage of V3-V4 (red line) grows as α increases. (d) At the same $\alpha = 45°$, when d decreases, the voltage of V3-V4 increases at d=0.10 BL regardless of sliding speed.

Windsor *et al.* measured the kinematics of blind Mexican cave fish, and found that the fish reacted to avoid collision with the wall at a distance of 0.108 BL [33]. Through simulation and PIV experiments, they further illustrated that the stimuli to the lateral line, especially on the head, seemed to be sufficient for fish to detect the walls when the distance was within 0.1 BL, when the fish was gliding parallel to a wall or toward to a wall [23], [25]. In the passive hydrodynamic experiments, P1, P2, and V4 can respond to the wall within 0.1 BL. In the active hydrodynamic experiments, V3-V4 can respond within 0.1 BL. The results indicate that our ALL system with optimized layout achieves a similar hydrodynamic imaging ability for wall detection. In addition to attitude control, the optimized sensor placement shows the potential to be used in underwater robots for obstacle avoidance.

IV. Discussion

A. Advantages of Sensor Fusion

In our previous work [10], we demonstrated the advantages of pressure and flow velocity sensor fusion in underwater source localization. The fusion of multimodal sensors can extend the detection range in 3D space and compensate for the blind area of a single sensing modality. In this study, we focused on the placement of sensors on the 3D model. Due to the significant sensor variations in yaw angle (Fig. 11) and wall detection (Fig. 13, Fig. 14), we did not apply complex sensor fusion algorithms.

The experimental results directly demonstrated the complementation of differential pressure and flow velocity sensors. For example, during yaw angle experiments, V6 suffered from reflux applied on the leeward side (Fig. 11(b)); however, it responded to the wall in passive hydrodynamic experiments (Fig. 13(b)). In contrast, P1 could distinguish yaw angle well (Fig. 11(a)) but changed insignificantly in wall detection (Fig. 13(a)). V4 performed well in both experiments. Although only a few sensors changed significantly in yaw angle detection or wall detection, sensor fusion is crucial for the ALL system to enhance the underwater detection capability under various working conditions.

The fusion of pressure and flow velocity can also compensate for the detection limits of a single sensing modality. At a low flow velocity, the impact of water is small, and the differential pressure does not significantly change (only a few pascals); however, the sensitivity of the flow velocity sensor is high at low speeds (Fig. 9). When the flow velocity is high and the impact is significant, the sensitivity of the flow velocity sensor with logarithmic fitting curve decreases, but the linear differential pressure sensor works properly (Fig. 7).

B. Generalization of Placement Strategy

The results obtained by the maximized hydrodynamic simulation were similar to the biological lateral line distribution of blind fish, indicating that the lateral line system distribution of fish is affected by hydrodynamics. This strategy can inspire the study of biological lateral lines and help explore the relationship between hydrodynamic parameters, fish shape, and lateral line system distribution.

Our method can be extended to other underwater robots. Because the model itself will affect the 3D spatial flow field, iterative optimization algorithms for 2D models become considerably complex or unavailable. Based on mature computational fluid dynamics, the maximization hydrodynamic simulation strategy can be applied to high-fidelity 3D models, and the sensor placement area can be qualitatively obtained through simple data processing. In addition to pressure and flow velocity sensors, other sensors can be placed on the model based on the simulation results of the corresponding hydrodynamic parameters.

V. Conclusion

In this study, we designed an artificial lateral line system with an optimized sensor placement by using a maximized hydrodynamic stimulation strategy. Differential pressure sensors and hot-film flow velocity sensors were installed on a bionic fish model to simulate the CNs and SNs, respectively, of biological lateral lines. The results of simulation and experiments of yaw angle detection indicated that the optimized sensor placement based on our maximized hydrodynamic stimulation strategy was consistent with the biological lateral line distribution. Both passive and active wall detection experiments were conducted. The ALL system with optimized sensor placement was found to respond to the wall within 0.1 BL, comparable to the sensing capability of a blind cave fish. The strategy can be used to place multiple sensors on the 3D models and has potential applications in robotic fish and other underwater vehicles.

This study demonstrated that the fusion of differential pressure sensors and flow velocity sensors could complement the detection limits of a single sensing modality. However, the true fusion application of different sensing modalities has not yet been achieved. In future work, we aim to design a robotic fish with an optimized ALL system and a deep fusion of pressure and flow velocity sensors.

References

[1] S. Coombs, P. Görner, and H. Münz, *The Mechanosensory Lateral Line: Neurobiology and Evolution*. Berlin, Germany: Springer, 2012.

[2] M. Yoshizawa, Š. Gorički, D. Soares, and W. R. Jeffery, "Evolution of a behavioral shift mediated by superficial neuromasts helps cavefish find food in darkness," *Curr. Biol.*, vol. 20, no. 18, pp. 1631–1636, Sep. 2010.

[3] D. Soares and M. Niemiller, "Variation in cephalic neuromasts surface and cave-dwelling fishes of the family Amblyopsidae (Teleostei: Percopsiformes)," *J. Cave Karst Stud.*, vol. 82, no. 3, pp. 198–209, Sep. 2020.

[4] Y. Yang *et al.*, "Artificial lateral line with biomimetic neuromasts to emulate fish sensing," *Bioinspiration Biomimetics*, vol. 5, no. 1, Mar. 2010, Art. no. 016001.

[5] A. T. Abdulsadda and X. Tan, "Nonlinear estimation-based dipole source localization for artificial lateral line systems," *Bioinspiration Biomimetics*, vol. 8, no. 2, Mar. 2013, Art. no. 026005.

[6] T. Salumäe and M. Kruusmaa, "Flow-relative control of an underwater robot," *Proc. Roy. Soc. A, Math., Phys. Eng. Sci.*, vol. 469, no. 2153, May 2013, Art. no. 20120671.

[7] L. D. Chambers *et al.*, "A fish perspective: Detecting flow features while moving using an artificial lateral line in steady and unsteady flow," *J. Roy. Soc. Interface*, vol. 11, no. 99, Oct. 2014, Art. no. 20140467.

[8] J. F. Fuentes-Pérez, "Current velocity estimation using a lateral line probe," *Ecological Eng.*, vol. 85, pp. 296–300, 2015.

[9] J. F. Fuentes-Perez, K. Kalev, J. A. Tuhtan, and M. Kruusmaa, "Underwater vehicle speedometry using differential pressure sensors: Preliminary results," in *Proc. IEEE/OES Auton. Underwater Veh.*, Nov. 2016, pp. 156–160.

[10] Y. Jiang *et al.*, "Underwater source localization using an artificial lateral line system with pressure and flow velocity sensor fusion," *IEEE/ASME Trans. Mechatronics*, to be published, doi: 10.1109/TMECH.2021.3062869

[11] B. J. Wolf, S. Warmelink, and S. M. van Netten, "Recurrent neural networks for hydrodynamic imaging using a 2D-sensitive artificial lateral line," *Bioinspiration Biomimetics*, vol. 14, no. 5, Jul. 2019, Art. no. 055001.

[12] D. Xu, Z. Lv, H. Zeng, H. Bessaih, and B. Sun, "Sensor placement optimization in the artificial lateral line using optimal weight analysis combining feature distance and variance evaluation," *Int. Soc. Automat. Trans.*, vol. 86, pp. 110–121, Mar. 2019.

[13] D. Xu, Y. Zhang, J. Tian, H. Fan, Y. Xie, and W. Dai, "Optimal sensor placement of the artificial lateral line for flow parametric identification," *Sensors*, vol. 21, no. 12, p. 3980, Jun. 2021.

[14] P. Weber, G. Arampatzis, G. Novati, S. Verma, C. Papadimitriou, and P. Koumoutsakos, "Optimal flow sensing for schooling swimmers," *Biomimetics*, vol. 5, no. 1, p. 10, Mar. 2020.

[15] A. Ahrari, H. Lei, M. A. Sharif, K. Deb, and X. Tan, "Reliable underwater dipole source characterization in 3D space by an optimally designed artificial lateral line system," *Bioinspiration Biomimetics*, vol. 12, no. 3, Apr. 2017, Art. no. 036010.

[16] W. Wang, Y. Li, X. Zhang, C. Wang, S. Chen, and G. Xie, "Speed evaluation of a freely swimming robotic fish with an artificial lateral line," in *Proc. IEEE Int. Conf. Robot. Automat.*, 2016, pp. 4737–4742.

[17] W.-K. Yen, D. M. Sierra, and J. Guo, "Controlling a robotic fish to swim along a wall using hydrodynamic pressure feedback," *IEEE J. Ocean. Eng.*, vol. 43, no. 2, pp. 369–380, Apr. 2018.

[18] A. Romero and S. M. Green, "The end of regressive evolution: Examining and interpreting the evidence from cave fishes," *J. Fish Biol.*, vol. 67, no. 1, pp. 3–32, Jul. 2005.

[19] Y.-H. Zhao, R. E. Gozlan, and C.-G. Zhang, "Out of sight out of mind: Current knowledge of Chinese cave fishes," *J. Fish Biol.*, vol. 79, no. 6, pp. 1545–1562, Dec. 2011.

[20] Y. Jiang, J. Fu, D. Zhang, and Y. Zhao, "Investigation on the lateral line systems of two cavefish: Sinocyclocheilus Macrophthalmus and S. Microphthalmus (Cypriniformes: Cyprinidae)," *J. Bionic Eng.*, vol. 13, no. 1, pp. 108–114, Mar. 2016.

[21] Z. Ma, H. Herzog, Y. Jiang, Y. Zhao, and D. Zhang, "Exquisite structure of the lateral line system in eyeless cavefish Sinocyclocheilus tianlinensis contrast to eyed Sinocyclocheilus macrophthalmus (Cypriniformes: Cyprinidae)," *Integrative Zoology*, vol. 15, pp. 314–328, 2020.

[22] A. Gao and M. Triantafyllou, "Bio-inspired pressure sensing for active yaw control of underwater vehicles," Ph.D. dissertation, Dept. Mech. Eng., Massachusetts Inst. Technol., IEEE, Hampton Roads, VA, Oct. 2012.

[23] S. P. Windsor, S. E. Norris, S. M. Cameron, G. D. Mallinson, and J. C. Montgomery, "The flow fields involved in hydrodynamic imaging by blind Mexican cave fish (Astyanax fasciatus). Part II: Gliding parallel to a wall," *J. Exp. Biol.*, vol. 213, no. 22, pp. 3832–3842, Nov. 2010.

[24] L. Ristroph, J. C. Liao, and J. Zhang, "Lateral line layout correlates with the differential hydrodynamic pressure on swimming fish," *Phys. Rev. Lett.*, vol. 114, no. 1, Jan. 2015, Art. no. 018102.

[25] S. P. Windsor, S. E. Norris, S. M. Cameron, G. D. Mallinson, and J. C. Montgomery, "The flow fields involved in hydrodynamic imaging by blind Mexican cave fish (Astyanax fasciatus). Part I: Open water and heading towards a wall," *J. Exp. Biol.*, vol. 213, no. 22, pp. 3819–3831, Nov. 2010.

[26] X. Zheng *et al.*, "Underwater positioning based on an artificial lateral line and a generalized regression neural network," *J. Bionic Eng.*, vol. 15, no. 5, pp. 883–893, Sep. 2018.

[27] G. Liu, S. Gao, T. Sarkodie-Gyan, and Z. Li, "A novel biomimetic sensor system for vibration source perception of autonomous underwater vehicles based on artificial lateral lines," *Meas. Sci. Technol.*, vol. 29, no. 12, Dec. 2018, Art. no. 125102.

[28] J. F. Fuentes-Pérez, "Flow sensing with pressure sensor-based artificial lateral lines: From the laboratory to the field," Ph.D. dissertation, Tallinn Univ., Sep. 2019.

[29] J. T. W. Kuo, L. Yu, and E. Meng, "Micromachined thermal flow sensors," *Micromachines*, vol. 3, no. 3, pp. 550–573, Jul. 2012.

[30] B. Sun, P. Wang, J. Luo, J. Deng, S. Guo, and B. Ma, "A flexible hot-film sensor array for underwater shear stress and transition measurement," *Sensors*, vol. 18, no. 10, p. 3469, Oct. 2018.

[31] D. M. Bot, B. J. Wolf, and S. M. van Netten, "The quadrature method: A novel dipole localisation algorithm for artificial lateral lines compared to state of the art," *Sensors*, vol. 21, no. 13, p. 4558, Jul. 2021.

[32] P. Duraisamy, R. K. Sidharthan, and M. N. Santhanakrishnan, "Design, modeling, and control of biomimetic fish robot: A review," *J. Bionic Eng.*, vol. 16, no. 6, pp. 967–993, Nov. 2019.

[33] S. P. Windsor, D. Tan, and J. C. Montgomery, "Swimming kinematics and hydrodynamic imaging in the blind Mexican cave fish (Astyanax fasciatus)," *J. Exp. Biol.*, vol. 211, no. 18, pp. 2950–2959, Sep. 2008.